A&A 598, A114 (2017)
DOI: 10.1051/0004-6361/201629213

Astronomy & Astrophysics

Bars as seen by *Herschel* and Sloan

Guido Consolandi[1], Massimo Dotti[1], Alessandro Boselli[2], Giuseppe Gavazzi[1], and Fabio Gargiulo[1]

[1] Dipartimento di Fisica G. Occhialini, Università di Milano-Bicocca, Piazza della Scienza 3, 20126 Milano, Italy
e-mail: guido.consolandi@mib.infn.it
[2] Aix Marseille Université, CNRS, LAM (Laboratoire d'Astrophysique de Marseille), UMR 7326, 13388 Marseille, France

Received 30 June 2016 / Accepted 30 December 2016

ABSTRACT

We present an observational study of the effect of bars on the gas component and on the star formation properties of their host galaxies in a statistically significant sample of resolved objects, the *Herschel* Reference Sample. The analysis of optical and far-infrared images allows us to identify a clear spatial correlation between stellar bars and the cold-gas distribution mapped by the warm dust emission. We find that the infrared counterparts of optically identified bars are either bar-like structures or dead central regions in which star formation is strongly suppressed. Similar morphologies are found in the distribution of star formation directly traced by Hα maps. The sizes of such optical and infrared structures correlate remarkably well, hinting at a causal connection. In the light of previous observations and of theoretical investigations in the literature, we interpret our findings as further evidence of the scenario in which bars drive strong inflows toward their host nuclei: young bars are still in the process of perturbing the gas and star formation clearly delineates the shape of the bars; old bars on the contrary already removed any gas within their extents, carving a dead region of negligible star formation.

Key words. galaxies: structure – galaxies: star formation – galaxies: evolution

1. Introduction

Stellar bars are common features in disk galaxies on a broad range of stellar masses and local environments (e.g., Jogee et al. 2004; Sheth et al. 2008; Barazza et al. 2008; Nair & Abraham 2010; Masters et al. 2012; Skibba et al. 2012; Méndez-Abreu et al. 2012; Gavazzi et al. 2015). Because of their elongated shape, bars can exert a significant gravitational torque onto the host galaxy stellar and gaseous components, making these features one of the main drivers of galactic evolution (see e.g., Kormendy & Kennicutt 2004; Kormendy 2013; Sellwood 2014, for recent reviews). In particular, the interaction between the bar and the interstellar medium (ISM) within the bar extent results in fast inflows of gas toward the galactic center (Sanders & Huntley 1976; Roberts et al. 1979; Athanassoula 1992; Sakamoto et al. 1999). Such inflows can trigger nuclear bursts of star formation (SF; as observationally confirmed by Ho et al. 1997; Martinet & Friedli 1997; Hunt & Malkan 1999; Jogee et al. 2005; Laurikainen et al. 2010), and, if the gas infall proceeds unimpeded, accretion episodes onto the central massive black hole (if present, e.g., Shlosman et al. 1989; Berentzen et al. 1998).

Only recently, Verley et al. (2007), Cheung et al. (2013), Gavazzi et al. (2015), and Fanali et al. (2015) suggested that prompt gas removal, if converted into stars on the short dynamical timescale of the galaxy nucleus, quenches any SF in the central few kpc region of the galaxy. This scenario has strong implications for the evolution of the SF rate (SFR) observed in field disk galaxies as a function of their stellar mass, with the decline of the specific SFR (sSFR) observed in massive galaxies possibly linked to the formation of a stellar bar (Gavazzi et al. 2015; Consolandi et al. 2016). On the other hand, even if bars do not remove all the gas within their extent, they are expected to perturb the gas kinematics by pumping turbulence in the ISM, preventing the gas from fragmenting and decreasing the central SFR (e.g., Reynaud & Downes 1998; Haywood et al. 2016).

In order to test the two abovementioned scenarios, in this study we aim at mapping the distribution of gas in barred and unbarred galaxies. The most direct probe would require the direct imaging of molecular and neutral atomic gas. Unfortunately, such information is available only for a very limited sample of galaxies, and is often affected by either an angular resolution that is too low or a very limited field of view. However, these problems can be overcome because the molecular gas distribution correlates strongly with the distribution of the cold dust component (Boselli et al. 2002). We take full advantage of such leverage by using the far-infrared (FIR) images from the *Herschel* Reference Survey (HRS; Boselli et al. 2010). We compare the *Herschel* data with the optical images from the Sloan Digital Sky Survey (SDSS; York et al. 2000). We study the correlation between the occurrence of bars in optical images and that of either bar-like structures or central zones of no emission in the HRS. We further measure the extent of such optical and infrared structures and check whether they are correlated. For galaxies showing both an optical bar and an infrared bar-related structure we link their morphology to the star formation distribution as traced by Hα images (Kennicutt 1998). Finally a qualitative comparison to the few available HI maps tracing the atomic gas distribution is accomplished owing to the high resolution maps from the VIVA survey (Chung et al. 2009).

2. The *Herschel* Reference Sample

The galaxies analyzed in this work have been extracted from the *Herschel* Reference Survey, which is a volume-limited ($15 \leq D \leq 25$ Mpc), K-band-selected sample of nearby galaxies spanning a wide range of morphological types, ranging from ellipticals to

dwarf irregulars, and stellar masses ($10^8 \lesssim M_* \lesssim 10^{11}\ M_\odot$); the galaxies have been observed in guaranteed time with *Herschel* (Boselli et al. 2010).

Since the present work aims at performing a visual comparison of the ISM and the stellar morphology in the HRS galaxies, we need a sufficient spatial resolution in both the IR and the optical images as well as good sensitivity and little dust obscuration in the optical band. For this purpose we characterize the morphological properties of the stellar component and the ISM via the SDSS images in the *i* band (Cortese et al. 2012) and the 160 μm maps obtained with the PACS instrument (Cortese et al. 2014), respectively. At 160 μm the resolution is $FWHM = 11.4$ arcsec, while the pixel size of the reduced maps is 2.85 arcsec pixel^{-1} (Cortese et al. 2014). This photometric band was chosen among those available for the whole sample galaxies (22 μm from WISE; Ciesla et al. 2014; 100–500 μm, Ciesla et al. 2012; Cortese et al. 2014) as the best compromise in terms of sensitivity, angular resolution, and dust temperature. At this frequency, the FIR emission gives the distribution of the cold dust component, which is a direct tracer of the molecular gas phase of the ISM (e.g. Boselli et al. 2002) from galactic to sub-kpc scales (Corbelli et al. 2012; Smith et al. 2012; Bolatto et al. 2013; Sandstrom et al. 2013). On the optical side, the *i* band is only little affected by dust, is the best SDSS tracer of the stellar mass of a galaxy, and is preferred to the *z* band for its higher sensitivity; however, the Hα data are taken from Boselli et al. (2015). The SDSS, PACS, and Hα images are available on the HeDaM database[1].

Further on, we limited the analysis to the 261 late-type galaxies of the sample to avoid contamination from slow rotators (namely ellipticals, which do not develop bars; Sellwood 2014) and from early-type disks (including S0s) that have too little cold gas to test the bar-related quenching process (Boselli et al. 2014). Finally, we exclude galaxies with axis ratio that are lower than 0.4 to avoid a major inclination bias in our morphology classification and measures, leaving a final subsample of 165 late-type face-on galaxies.

3. Results

For each galaxy we visually inspect the *i*-band SDSS images and look for the presence of an evident stellar bar. Separately, we also visually inspect the PACS images in search of a central carved region with little to no emission, which, when present, is distributed along a bar-like component (see Fig. 1, HRS208) or in a small nuclear region surrounded by a ring-like structure (see Fig. 1, HRS220). In Fig. 1, from left to right, we show three illustrative cases representing the infrared morphologies possibly associated with optical bars (Cols. 1 and 2, HRS 208 and 220) and a normal spiral galaxy (last column, HRS 254). For each galaxy we give from top to bottom the SDSS RGB, the 160 μm, the continuum-subtracted Hα images, and the HI map from the VIVA survey (Chung et al. 2009), of which unfortunately only a few galaxies overlap our sample.

We find 51 barred galaxies (≈30% of the sample) in the *i* band, out of which 75% show an elliptical/circular area in the corresponding 160 μm images, where the only emission is distributed on a bar- or ring-like structure. On the other hand, we find 63 galaxies (≈38% of the sample) hosting the described morphologies in the 160 μm images out of which 38 (≈65%) galaxies are found barred in the corresponding optical image. The frequency of galaxies hosting an infrared feature, which also shows a corresponding optical bar, and the occurrence of optical bars, which reveals an infrared feature, are ≈65% and ≈75%, respectively. These percentages rise to ≈85% and ≈96% if we include 16 galaxies classified as barred by other literature classifications found in the NASA Extragalactic Database (NED). These are mostly weak bars that are difficult to recognize visually and whose extent is difficult to quantify. For this reason we exclude these objects from our further analysis. In order to quantitatively relate the region of star formation avoidance to the presence of an optical bar, we measure the size of these structures visually in the optical and 160 μm and then do the same using ellipse fits to isophotes. The two approaches are useful because the eye can effectively recognize features and their extent even if somewhat subjective, while ellipse fits are objective measures that nevertheless can be strongly affected by other structures in the galaxies. Four of the authors (GC, MD, FG, and GG) manually evaluated the extent of optical bars by measuring the radius of the circular region circumscribing the bar, avoiding possible HII regions at the edges of the bar. On the other hand, we measure the radius of the circle circumscribing the bar when an infrared bar is present in the 160 μm images, while we measure the inner semimajor axis of the ring-like structure surrounding the depleted region when no clear bar is discernible (as depicted in Fig. 1). For optical bars showing the region of avoidance in the 160 μm images we also visually inspect the continuum-subtracted Hα images finding similar morphologies and repeat the same measure.

We use IRAF[2] task *ellipse* to measure ellipticity (ϵ) and position angle (PA) radial profiles of the isophotes of each sample galaxy in each considered band. In optical broadbands, it is well tested that the radius at which there is a peak in the ellipticity profile and a related plateau in the PA profile is a good proxy for the extension of the bar (Jogee et al. 2004; Laurikainen et al. 2010; Consolandi 2016). Following this procedure we extract a radius of the bar in the *i*-band for each galaxy and, we deduce the bars strength following (Laurikainen et al. 2007) from the peak of the ϵ profile in the *i* band. We find that ≈95% of the galaxies that we classified as barred harbor strong bars ($\epsilon > 0.4$). Although this quantitative method has not been applied to FIR data previously, ellipse fits can nevertheless be derived for the 160 μm images and the ϵ and PA profiles examined for a bar signature. Since we are trying to measure a region of decreased emission possibly surrounded by a ring-like emitting structure, we also extract a radial surface brightness profile from concentric elliptical apertures centered on the galaxy and ellipticity fixed to the outer infrared isophotes. The derived surface brightness profile therefore has a relative maximum in correspondence of the ring-like structure. In the cases where no infrared bar is discernible, the radius at which this occurs is a good proxy of the extension of the nonemitting region.

In the 160 μm images, this method succeeds to extract the radius of the nonemitting region or of the bar in 75% of the barred galaxies. Because of the irregular and clumpy distribution of light at 160 μm, the fit of the isophotes does not converge in 25% of the galaxies. Therefore, to preserve the statistics of our already limited sample, in Fig. 2 we plot the radius obtained by averaging the measures of the optical bars made by the authors versus those from the 160 μm data (black empty dots) and those from the continuum-subtracted Hα images (red empty dots). All radii are normalized to the *i*-band 25th mag isophote radius of the galaxy, taken from Cortese et al. (2012), and errors are evaluated

[1] http://hedam.lam.fr/

[2] IRAF (Image Reduction and Analysis Facility) is a software for the reduction and analysis of astronomical data.

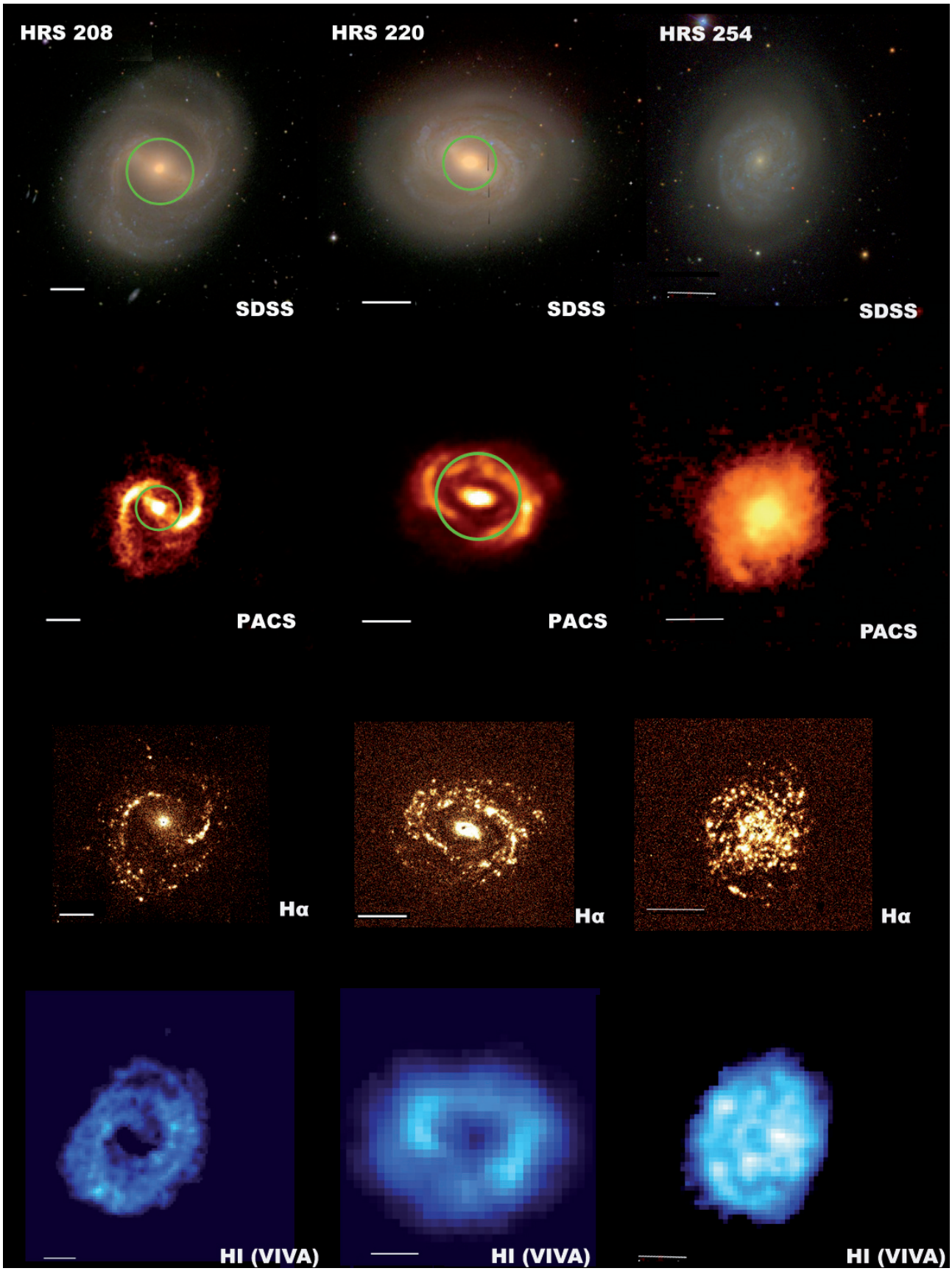

Fig. 1. Examples for the categories classified in this work. *From left to right*: NGC 4548 (HRS-208), NGC 4579 (HRS-220), and NGC 4689 (HRS-256). The *top row* shows the SDSS RGB image of the galaxy while the *second row* shows the corresponding PACS images. The green circles qualitatively illustrate the circular region used to measure the extensions of structures. The Hα image is reported in the *third row* and the HI map from the VIVA survey is reported in the *fourth row*. In each frame a 1 arcminute scale is given.

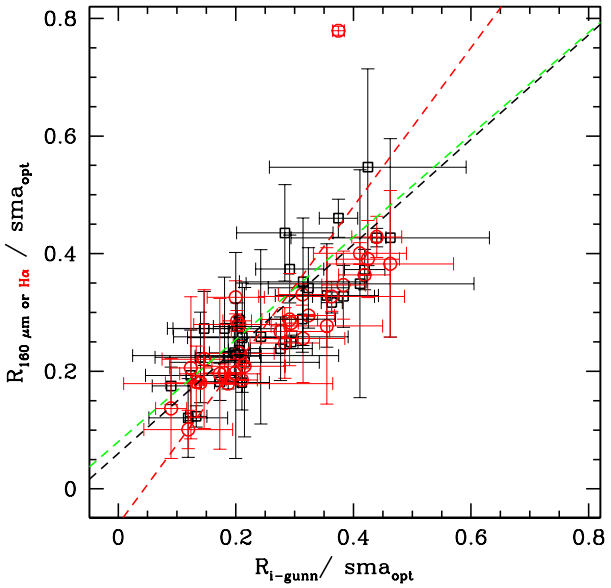

Fig. 2. Comparison between the radii of bars in the i band and the radii of the central zone of avoidance of the 160 μm (black dots) and continuum-subtracted Hα (red dots) images. The black and red dashed lines represent the bisector regression to the i band vs. 160 μm and i band vs. Hα data, respectively. The green dashed line is the linear fit to the i band versus 160 μm radii measured using *ellipse* in IRAF for 75% of the sample. All radii are normalized to the optical diameter of the galaxy taken from Cortese et al. (2012). A comparison between the visual and automatic optical and 160 μm radii is available in Appendix A.

from the standard deviation of our measurements. The black and red dashed lines indicate the bisector fit (Isobe et al. 1990) to the data for the 160 μm (slope ~0.89 ± 0.11) and the Hα data (slope ~1.35 ± 0.08), respectively. The slope of the fit relative to the optical versus Hα data is strongly influenced by the extremely deviant point (associated with HRS 322) visible in Fig. 2. This outlier is characterized by a very small error, as all the authors consistently measured the same radius with very little scatter. We stress, however, that the semimajor axis of this galaxy in the Hα distribution is perpendicular to the optical bar (see the optical and Hα image in Appendix A) thus the important discrepancy is mostly due to projection effects. If we exclude this point from the fit, the slope becomes 0.79 ± 0.11. Finally, in green, we plot the best linear fit of the comparison of optical versus 160 μm radii measured with IRAF (slope ~0.87 ± 0.10). All fits show a strong consistency between them even when evaluated with independent methods. To further check a possible bias from inclination, we derived the same fits for a subsample of galaxies with axis ratios greater than 0.7 (≈40% of the sample), and find fully consistent results.

4. Discussion and conclusions

The study and comparison of frequencies of occurrence of bar-related features in the optical and FIR, as traced by stellar continuum and warm dust emission, respectively, results in a fraction of galaxies hosting an optical bar of ~30%, while a zone of avoidance with or without an infrared bar is found in 38% of the 160 μm images. The percentages of common occurrence suggests that FIR images are an effective way of identifying the presence of a bar in a galaxy.

For the galaxies hosting both an optical bar and a central zone of avoidance in the 160 μm images, we measured the angular size of both structures with independent methods, and find a good correspondence. First, we measured the extent of bars in optical images, while in the FIR images we measured the extent of the bar-like structure, if present, or of the inner semi-major axis of the ring-like structure. In the latter case, we stress that the projected angular sizes of the optical bar and the radius of nonemitting zone may differ significantly[3] depending on the bar orientation. In 75% of the barred galaxies we successfully ran the IRAF task *ellipse* to measure objectively the extent of these structures in both the i-band and 160 μm images, using the derived ellipticity, PA and surface brightness profiles. The goodness of the correlation strongly hints at a physical connection between the presence of an optical strong bar and a gas-depleted/quenched region where little SF is still possible. Star formation is only found in the very center, where the bar conveys the gas originally within its reach, or along the bar. Such an effect is consistent with what we see in the continuum-subtracted Hα images of the sample. Indeed, SF is distributed mainly in the nuclear region of galaxies and/or along the bar (consistent with Verley et al. 2007; see Fig. 1) and shows a morphology similar to that observed in the FIR.

We conclude that the FIR morphologies are similar to the Hα morphologies (consistent with Verley et al. 2007) and that both are consistent with bar-driven inflows of gas inside the corotation radius as predicted by simulations (Sanders & Huntley 1976; Athanassoula 1992). Figure 1 qualitatively shows that the HI emission as well, when avilable, shows similar morphologies. The impact on the cold gas component, as derived from the FIR, is consistent with what has been observed in a few galaxies (Sakamoto et al. 1999) and affects the star formation of barred galaxies (Verley et al. 2007; Gavazzi et al. 2015). As soon as a bar starts growing, the gas is initially perturbed and compressed along the bar, where it forms stars while gradually losing its angular momentum. As the time goes by, the gas is swept by the bar into sub-kpc scales, leaving a gas-depleted and SF quenched region of the size of the bar itself, with or without a central knot of SF, depending on the consumption timescale of the originally infalling gas.

Acknowledgements. We thank the anonymous referee for their constructive criticism. This research has been partly financed by the French national program PNCG, and has made use of the GOLDmine database (Gavazzi et al. 2003, 2014b) and SDSS Web site `http://www.sdss.org/`

References

Athanassoula, E. 1992, MNRAS, 259, 345
Barazza, F. D., Jogee, S., & Marinova, I. 2008, ApJ, 675, 1194
Berentzen, I., Heller, C. H., Shlosman, I., & Fricke, K. 1998, MNRAS, 300, 49
Bolatto, A. D., Wolfire, M., & Leroy, A. K. 2013, ARA&A, 51, 207
Boselli, A., Lequeux, J., & Gavazzi, G. 2002, A&A, 384, 33
Boselli, A., Eales, S., Cortese, L., et al. 2010, PASP, 122, 261
Boselli, A., Cortese, L., Boquien, M., et al. 2014, A&A, 564, A66
Boselli, A., Fossati, M., Gavazzi, G., et al. 2015, A&A, 579, A102
Cheung, E., Athanassoula, E., Masters, K. L., et al. 2013, ApJ, 779, 162
Chung, A., van Gorkom, J. H., Kenney, J. D. P., Crowl, H., & Vollmer, B. 2009, AJ, 138, 1741
Ciesla, L., Boselli, A., Smith, M. W. L., et al. 2012, A&A, 543, A161
Ciesla, L., Boquien, M., Boselli, A., et al. 2014, A&A, 565, A128
Consolandi, G. 2016, A&A, 595, A67
Consolandi, G., Gavazzi, G., Fumagalli, M., Dotti, M., & Fossati, M. 2016, A&A, 591, A38
Corbelli, E., Bianchi, S., Cortese, L., et al. 2012, A&A, 542, A32
Cortese, L., Boissier, S., Boselli, A., et al. 2012, A&A, 544, A101
Cortese, L., Fritz, J., Bianchi, S., et al. 2014, MNRAS, 440, 942

[3] Up to a factor of ≈2.5 for the maximum inclination of B/A = 0.4 allowed in our sample.

Fanali, R., Dotti, M., Fiacconi, D., & Haardt, F. 2015, MNRAS, 454, 3641
Gavazzi, G., Boselli, A., Donati, A., Franzetti, P., & Scodeggio, M. 2003, A&A, 400, 451
Gavazzi, G., Franzetti, P., & Boselli, A. 2014, ArXiv e-prints [arXiv:1401.8123]
Gavazzi, G., Consolandi, G., Dotti, M., et al. 2015, A&A, 580, A116
Haywood, M., Lehnert, M. D., Di Matteo, P., et al. 2016, A&A, 589, A66
Ho, L. C., Filippenko, A. V., & Sargent, W. L. W. 1997, ApJ, 487, 591
Hunt, L. K., & Malkan, M. A. 1999, ApJ, 516, 660
Isobe, T., Feigelson, E. D., Akritas, M. G., & Babu, G. J. 1990, ApJ, 364, 104
Jogee, S., Barazza, F. D., Rix, H.-W., et al. 2004, ApJ, 615, L105
Jogee, S., Scoville, N., & Kenney, J. D. P. 2005, ApJ, 630, 837
Kennicutt, R. C., Jr. 1998, ARA&A, 36, 189
Kormendy, J. 2013, in Secular Evolution of Galaxies (Cambridge, UK: Cambridge University Press), 1
Kormendy, J., & Kennicutt, R. C., Jr. 2004, ARA&A, 42, 603
Laurikainen, E., Salo, H., Buta, R., & Knapen, J. H. 2007, MNRAS, 381, 401
Laurikainen, E., Salo, H., Buta, R., Knapen, J. H., & Comerón, S. 2010, MNRAS, 405, 1089
Martinet, L., & Friedli, D. 1997, A&A, 323, 363
Masters, K. L., Nichol, R. C., Haynes, M. P., et al. 2012, MNRAS, 424, 2180
Méndez-Abreu, J., Sánchez-Janssen, R., Aguerri, J. A. L., Corsini, E. M., & Zarattini, S. 2012, ApJ, 761, L6
Nair, P. B., & Abraham, R. G. 2010, ApJ, 714, L260
Reynaud, D., & Downes, D. 1998, A&A, 337, 671
Roberts, W. W., Jr., Huntley, J. M., & van Albada, G. D. 1979, ApJ, 233, 67
Sanders, R. H., & Huntley, J. M. 1976, ApJ, 209, 53
Sandstrom, K. M., Leroy, A. K., Walter, F., et al. 2013, ApJ, 777, 5
Sakamoto, K., Okumura, S. K., Ishizuki, S., & Scoville, N. Z. 1999, ApJ, 525, 691
Sheth, K., Elmegreen, D. M., Elmegreen, B. G., et al. 2008, ApJ, 675, 1141
Sellwood, J. A. 2014, Rev. Mod. Phys., 86, 1
Shlosman, I., Frank, J., & Begelman, M. C. 1989, Nature, 338, 45
Smith, M. W. L., Eales, S. A., Gomez, H. L., et al. 2012, ApJ, 756, 40
Skibba, R. A., Masters, K. L., Nichol, R. C., et al. 2012, MNRAS, 423, 1485
Verley, S., Combes, F., Verdes-Montenegro, L., Bergond, G., & Leon, S. 2007, A&A, 474, 43
York, D. G., Adelman, J., Anderson, J. E., Jr., et al. 2000, AJ, 120, 1579

Appendix A: Additional figures

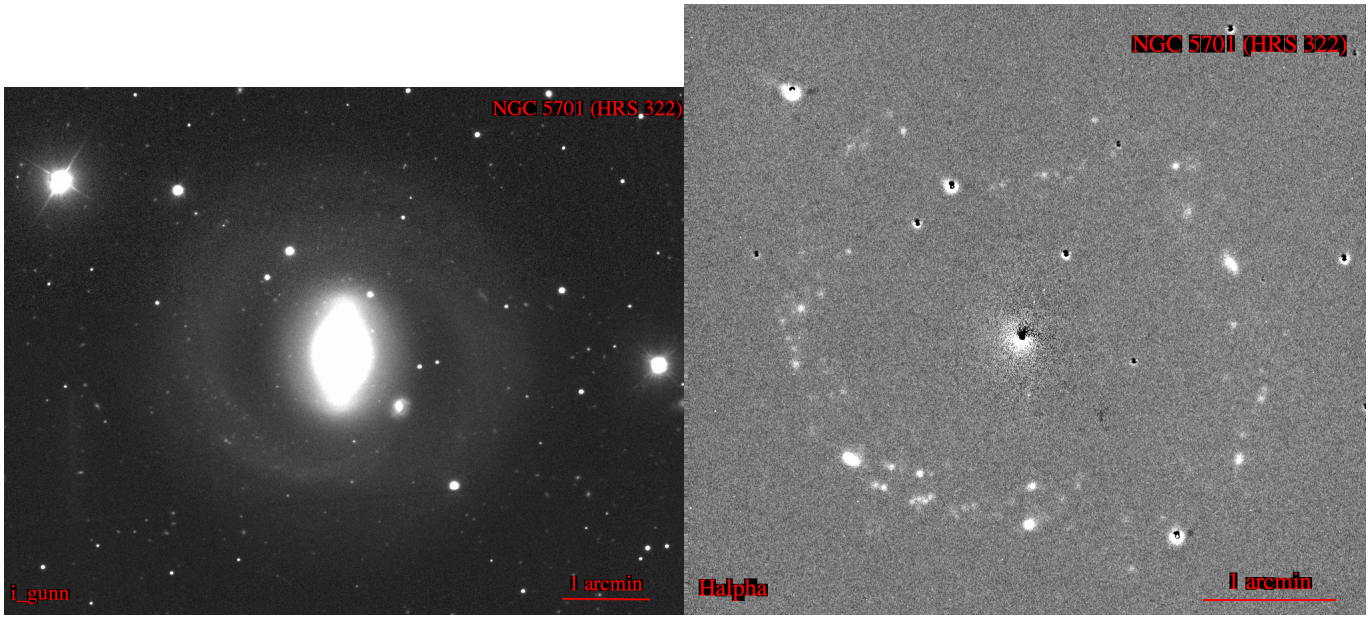

Fig. A.1. A barred galaxy NGC-5701 (HRS 322) representing the most deviant point of Fig. 2 observed in the *i* band (*left*) and in Hα (*right*). A 1 arcminute scale is given in both images.

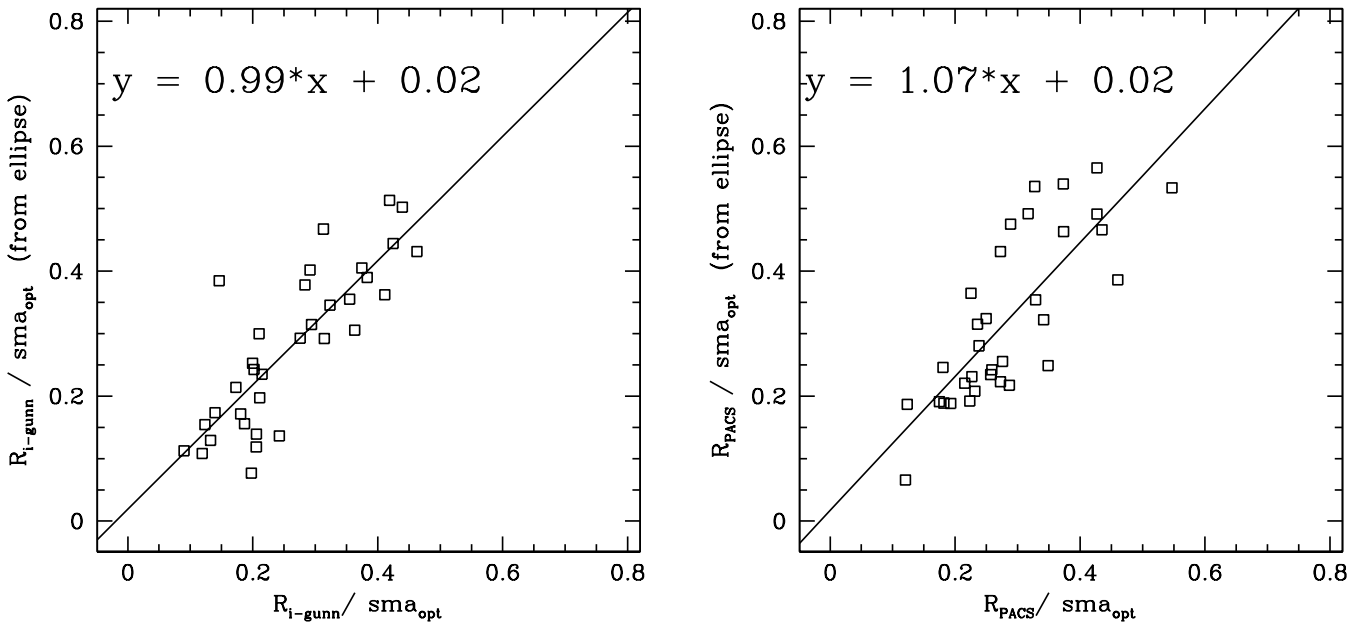

Fig. A.2. A comparison between the average radius measured by the authors (*x*-axis) and the one measured using the IRAF task *ellipse* (*y*-axis) in the optical (*left*) and FIR (*right*) images. All radii are normalised to the optical semimajor axis taken from Cortese et al. (2012). The solid lines represent the linear fits to the data. The analytic expression of the evaluated linear fit is displayed in the top left of both diagrams.